Adaptive Method of Lines for Magneto-Hydrodynamic PDE Models

PAUL A. ZEGELING
Mathematical Institute, Utrecht University
P.O. Box 80.010, 3508 TA, Utrecht The Netherlands
email: zegeling@math.uu.nl

RONY KEPPENS
F.O.M.-Institute for Plasma Physics 'Rijnhuizen'
P.O. Box 1207, 3430 BE, Nieuwegein The Netherlands
email: keppens@rijnh.nl

Abstract

An adaptive grid technique for use in the solution of multi-dimensional time-dependent PDEs is applied to several magnetohydrodynamic model problems. The technique employs the method-of-lines and can be viewed both in a continuous and semi-discrete setting. By using an equidistribution principle, it has the ability to track individual features of the physical solutions in the developing plasma flows. Moreover, it can be shown that the underlying grid varies smoothly in time and space. The results of several numerical experiments are presented which cover many aspects typifying nonlinear magneto-fluid dynamics.

1 Introduction

Many interesting phenomena in plasma fluid dynamics can be described within the framework of magneto-hydrodynamics (MHD). Numerical studies in plasma flows frequently involve simulations with highly varying spatial and temporal scales. As a consequence, numerical methods on uniform grids

may be inefficient to use, since a very large number of grid points is needed to resolve the spatial structures, such as shocks, contact discontinuities, shear layers, or current sheets. For the efficient study of these phenomena, we require adaptive grid methods which automatically track and spatially resolve one or more of these structures.

Over the years a large number of adaptive grid methods have been proposed for time-dependent PDE models. Two main strategies of adaptive grid methods can be distinguished, namely, static-regridding methods and moving-grid or dynamic-regridding methods. In static-regridding methods (denoted by h-refinement) the location of nodes is fixed. A method of this type adapts the grid by adding nodes where they are necessary and removing them when they are no longer needed. The refinement or de-refinement is controlled by error estimates or error monitor values (which have no resemblance with the true numerical error). Recent examples of these methods are described in [16], [4], [20], [7]. In dynamic-regridding methods (denoted by r-refinement) nodes are moving continuously in the space-time domain, like in classical Lagrangian methods, and the discretization of the PDE is coupled with the motion of the grid. Examples can be found in [3], [18], [19], [5], [8].

In this paper we follow the second approach. The adaptive grid method is based on a semi-discretization of a fourth-order PDE for the grid variable and is being coupled to the original MHD model re-written in a new co-ordinate system. We use the so-called Method-Of-Lines-technique (MOL) [11]: first we discretize the PDEs in the space direction using a finite-difference approximation, so as to convert the PDE problem into a system of stiff, ordinary differential equations (ODEs) with time as independent variable. The discretization in time of this stiff ODE system then yields the required fully discretized scheme.

The layout of the paper is as follows. In the next section we present the full set of MHD equations and their physical meaning. In section 3 we describe the restriction to the one-dimensional situation and the adaptive grid method. The moving grid is defined as the solution of an adaptive grid PDE. Numerical experiments are shown for three different cases: an MHD-shocktube model, a problem describing Shear-Alfvén wave propagation, and an oscillating plasma sheet in vacuum surroundings. Section 4 discusses the essential elements for generalizing the MOL approach to multi-dimensional MHD simulations. We evaluate different means for 2D grid adaptation on kinematic magnetic field models, with particular attention

paid to the solenoidal condition on the magnetic field vector. Section 5 lists our conclusions and presents an outlook to future work.

2 The equations of magnetohydrodynamics

The MHD equations govern the dynamics of a charge-neutral 'plasma'. Just like the conservative Euler equations provide a continuum description for a compressible gas, the MHD equations express the basic physical conservation laws to which a plasma must obey. Because plasma dynamics is influenced by magnetic fields through the Lorentz-force, the needed additions in going from hydrodynamic to magneto-hydrodynamic behaviour is a vector equation for the magnetic field evolution and extra terms in the Euler system that quantify the magnetic force and energy density.

Using the conservative variables density ρ, momentum density $\mathbf{m} \equiv \rho\mathbf{v}$ (with velocity $\mathbf{v}$), magnetic field $\mathbf{B}$, and total energy density e, the ideal MHD equations can be written as follows (cfr. [2], [13], [15]):

Conservation of mass:

$$\frac{\partial \rho}{\partial t} + \nabla \cdot (\rho \mathbf{v}) = 0. \tag{1}$$

Conservation of momentum:

$$\frac{\partial (\rho \mathbf{v})}{\partial t} + \nabla \cdot (\rho \mathbf{v}\mathbf{v} - \mathbf{B}\mathbf{B}) + \nabla p_{tot} = 0. \tag{2}$$

Conservation of energy:

$$\frac{\partial e}{\partial t} + \nabla \cdot (e\mathbf{v} + \mathbf{v}p_{tot} - \mathbf{B}\mathbf{B} \cdot \mathbf{v}) = 0 \quad \left[+ \epsilon_m (\nabla \times \mathbf{B})^2 \right]. \tag{3}$$

Magnetic field induction equation:

$$\frac{\partial \mathbf{B}}{\partial t} + \nabla \cdot (\mathbf{v}\mathbf{B} - \mathbf{B}\mathbf{v}) = 0 \quad [+ \epsilon_m \Delta \mathbf{B}]. \tag{4}$$

In (2) and (3) the total pressure p_{tot} consists of both a thermal and a magnetic contribution as given by

$$p_{tot} = p + \frac{\mathbf{B}^2}{2}, \quad \text{where} \quad p = (\gamma - 1)(e - \rho\frac{\mathbf{v}^2}{2} - \frac{\mathbf{B}^2}{2}) \tag{5}$$

is the thermal pressure. This set of equations must be solved in conjunction with an important condition on the magnetic field $\mathbf{B}$, namely the non-existence of magnetic 'charge' or monopoles. Mathematically, it is easily demonstrated that this property can be imposed as an initial condition alone, since

$$\nabla \cdot \mathbf{B}|_{t=0} = 0 \Longrightarrow \nabla \cdot \mathbf{B}|_{t \geq 0} = 0. \tag{6}$$

In multi-dimensional numerical MHD, the combined spatio-temporal discretization may not always ensure this conservation of the solenoidal character of the vector magnetic field. When dealing with a two-dimensional model problem for $\mathbf{B}$-evolution in section 4.2.6, we pay particular attention to this matter.

The terms between brackets in equations (3) and (4) extend the ideal MHD model with the effects of Ohmic heating due to the presence of currents. With the resistivity $\epsilon_m \neq 0$, we then solve the resistive MHD equations. Likewise, extra non-conservative source terms may be added to the momentum and energy equation for describing viscous effects. In the numerical experiments, we resort to artificial diffusive terms which can be thought of as approximations representing these actual physical phenomena.

3 Adaptive grid simulations for 1D MHD

3.1 The MHD equations in 1D

If we restrict the MHD model (1)–(6) to 1.5D, i.e. variations in one spatial x-dimension but possibly non-vanishing y-components for the vector quantities with $\partial/\partial y = 0$, we obtain a 5-component PDE system which is formally written as

$$\frac{\partial \mathbf{\Psi}}{\partial t} + \frac{\partial \mathbf{F}(\mathbf{\Psi})}{\partial x} = 0, \qquad x \in [x_L, x_R], \quad t > 0. \tag{7}$$

Here, $\mathbf{\Psi} = (\rho, m_1, m_2, B_2, e)^T$ is the vector of conserved variables (m_1, m_2 are now the x- and y-components of the momentum vector and B_2 denotes the y-component of the magnetic induction), with the flux-vector $\mathbf{F} = (F_1, ..., F_5)^T$ given by

$$\begin{aligned} F_1 &= m_1, \\ F_2 &= \frac{m_1^2}{\rho} - \bar{B}_1^2 + (\gamma - 1)e - (\gamma - 1)\frac{m_1^2 + m_2^2}{2\rho} + (2 - \gamma)\frac{\bar{B}_1^2 + B_2^2}{2}, \end{aligned}$$

$$
\begin{aligned}
F_3 &= \frac{m_1 m_2}{\rho} - \bar{B}_1 B_2, \\
F_4 &= B_2 \frac{m_1}{\rho} - \bar{B}_1 \frac{m_2}{\rho}, \\
F_5 &= \frac{m_1}{\rho}\left(\gamma e - (\gamma-1)\frac{m_1^2+m_2^2}{2\rho} + (2-\gamma)\frac{\bar{B}_1^2+B_2^2}{2}\right) - \bar{B}_1(\bar{B}_1\frac{m_1}{\rho} + B_2\frac{m_2}{\rho}).
\end{aligned}
$$

The constant γ is the ratio of specific heats and $\bar{B}_1$ is the constant first component of the magnetic induction vector. Indeed, in 1D model problems, the vanishing divergence of the magnetic field is thereby trivially satisfied. The remaining set of 5 PDEs given by (7) constitutes the physical model used for the 1D MHD simulations found below. We first indicate how this system is further manipulated and discretized to solve simultaneously for the adaptive grid with its corresponding solution.

3.2 The adaptive grid method in one space dimension

3.2.1 Transformation of variables

It is common practice in adaptive grid generation to submit the PDE model to a coordinate transformation. Ideally, the mapping should be chosen such that in the new coordinate variables the discretization error in the numerical solution is much smaller than in the original variables. In the new variables the PDEs are then simply uniformly partitioned. In general, applying a transformation

$$\xi = \xi(x,t) \in [0,1], \quad \theta = t, \tag{8}$$

to the system (7) gives after some elementary calculations

$$x_\xi \mathbf{\Psi}_\theta - \mathbf{\Psi}_\xi x_\theta + (\mathbf{F}(\mathbf{\Psi}))_\xi = 0. \tag{9}$$

Different choices for the transformation are possible. The coordinate transformation used in this paper is implicitly defined as the solution of a special partial differential equation (see sect. 3.2.2). Even without knowing this mapping, we can already semi-discretize (9) by noting that in the ξ-variable a uniform grid ($\xi_i = i/N,\ i = 0,...,N$) is imposed. Using central finite-differences, the PDEs (9) become a system of ODEs as follows:

$$(x_{i+1} - x_{i-1})\frac{\mathrm{d}\mathbf{\Psi}_i}{\mathrm{d}\theta} - (\mathbf{\Psi}_{i+1} - \mathbf{\Psi}_{i-1})\frac{\mathrm{d}x_i}{\mathrm{d}\theta} + \mathbf{F}(\mathbf{\Psi}_{i+1}) - \mathbf{F}(\mathbf{\Psi}_{i-1}) = 0 \qquad \forall i. \tag{10}$$

Note that we have multiplied (10) by the factor $2\Delta\xi$, which has a constant value by definition.

3.2.2 The adaptive grid PDE

We implicitly define the transformation $\xi(x,t)$, and thereby the grid distribution, as the solution of the following time-dependent 'adaptive grid PDE'

$$[(\mathcal{S}(x_\xi) + \tau x_{\xi\theta})\mathcal{W}]_\xi = 0. \tag{11}$$

The parameter $\tau > 0$ in (11) is a temporal smoothing parameter, the operator $\mathcal{S}$ incorporates a spatial smoothing in a manner detailed below, while

$$\mathcal{W} = \sqrt{1 + \sum_{j=1}^{5} \alpha_j (\mathbf{\Psi}_x^{(j)})^2}$$

is a weight function that depends on the derivatives of the different components $\mathbf{\Psi}^{(j)}$. The parameters α_j are termed 'adaptivity parameters'. Their values can be chosen to emphasize, if necessary, particular variables in the PDE model (such as the density or a magnetic field component for MHD problems). In full, the smoothing operator $\mathcal{S}$ in (11) is defined by

$$\mathcal{S} = \mathcal{I} - \sigma(\sigma+1)(\Delta\xi)^2 \frac{\partial^2}{\partial \xi^2}, \tag{12}$$

where $\sigma > 0$ is a spatial smoothing parameter and $\mathcal{I}$ the identity operator. This specific choice of transformation has several desirable properties, which are briefly discussed in sect. 3.2.3.

Since the adaptive grid PDE is fourth order in space, it is clear that we need four boundary conditions and one initial condition. An obvious choice is to take two Dirichlet and two Neumann conditions:

$$x|_{\xi=0} = x_L, \;\; x|_{\xi=1} = x_R, \;\; x_\xi|_{\xi=0} = x_\xi|_{\xi=1} = 0. \tag{13}$$

At initial time $\theta = 0$, the grid is uniformly distributed and is thus given by $x|_{\theta=0} = x_L + (x_R - x_L)\xi$.

3.2.3 Properties of the adaptive grid

It can be shown that the determinant of the Jacobian of the transformation implied by (11)–(12) satisfies the mesh-consistency condition

$$\mathcal{J} = x_\xi > 0 \quad \forall\, \theta \in [0,T], \;\; \forall \xi \in [0,1], \tag{14}$$

which in discretized form reads (since $\Delta\xi$ is a constant)

$$\Delta x_i(\theta) := x_i(\theta) - x_{i-1}(\theta) > 0 \quad \forall\ \theta \in [0,T]. \tag{15}$$

In other words, relation (15) states that the grid points can never cross one another (see chapter 4 in [18] and [5] for more details and proofs of these results). Another important property of the transformation satisfying (11)–(12) is the following:

$$\left|\frac{x_{\xi\xi}}{x_\xi}\right| \leq \frac{1}{\sqrt{\sigma(\sigma+1)\Delta\xi}}, \tag{16}$$

which may be translated in discrete terms as

$$\frac{1}{1+\frac{1}{\sigma}} \leq \frac{\Delta x_{i+1}(\theta)}{\Delta x_i(\theta)} \leq 1 + \frac{1}{\sigma} \quad \forall\ \theta \geq 0, \quad \forall i. \tag{17}$$

This property expresses 'local quasi-uniformity' and means that the variation in successive grid cells can be controlled by the parameter σ at every point in time.

A reasonable choice for the temporal smoothing parameter is $0 < \tau \leq 10^{-3} \times \{\text{timescale in PDE model}\}$, while the spatial smoothing parameter is typically $\sigma = \mathcal{O}(1)$. The adaptivity parameters are normally taken $\alpha_j = \mathcal{O}(1)$ (see also [18]), but may need re-scaling depending on the x-range and the magnitude of the individual $\mathbf{\Psi}^{(j)}$. Note that, if we switch off all smoothing in (11), we obtain the well-known 'equidistribution principle' which has both a continuous and discrete variant given by the formulae

$$\tau = \sigma = 0 \quad \Rightarrow \quad [x_\xi\, \mathcal{W}]_\xi = 0 \quad \forall\ \theta \in [0,T] \quad \Leftrightarrow \quad \xi(x,t) = \frac{\int_{x_L}^{x} \mathcal{W}\ \mathrm{d}\bar{x}}{\int_{x_L}^{x_R} \mathcal{W}\ \mathrm{d}\bar{x}}, \tag{18}$$

or in discretized form (using the midpoint rule for integration)

$$\Delta x_i \cdot \mathcal{W}_{i-1/2} = \text{constant} \quad \forall\ \theta \in [0,T]. \tag{19}$$

3.2.4 Semi-discretization of the adaptive grid PDE

The adaptive grid PDE (11) is semi-discretized using central-differences to obtain

$$[\tilde{\Delta} x_{i+1} + \tau \frac{\mathrm{d}\Delta x_{i+1}}{\mathrm{d}\theta}]\mathcal{W}_{i+1/2} - [\tilde{\Delta} x_i + \tau \frac{\mathrm{d}\Delta x_i}{\mathrm{d}\theta}]\mathcal{W}_{i-1/2} = 0 \quad \forall i, \tag{20}$$

where

$$\tilde{\Delta} x_i = \Delta x_i - \sigma(\sigma+1)(\Delta x_{i+1} - 2\Delta x_i + \Delta x_{i-1}), \tag{21}$$

which is a discretization of $\mathcal{S}(x_\xi)$ about the gridpoint $\xi_i = \frac{i}{N}$.

The discrete version of the weight function becomes

$$\mathcal{W}_{i-1/2} = \sqrt{1 + \sum_{j=1}^{5} \alpha_j (\mathbf{\Psi}^{(j)}_{x,i-1/2})^2}, \quad \text{with} \quad \mathbf{\Psi}^{(j)}_{x,i-1/2} = \frac{\mathbf{\Psi}^{(j)}_i - \mathbf{\Psi}^{(j)}_{i-1}}{\Delta x_i}. \tag{22}$$

The grid equations (20)–(21) are related to the adaptive grid described in [3]. The differences between (20)–(21) and [3] mainly consist of the use of cell-lengths instead of point concentrations and not applying the operator $\mathcal{S}$ to the $\frac{\mathrm{d}\Delta x}{\mathrm{d}\theta}$-terms. In compact notation the adaptive grid ODE system (20) reads

$$\tau\ \mathcal{B}(\mathbf{X}, \mathbf{\Psi}, \sigma, \alpha) \frac{\mathrm{d}\mathbf{X}}{\mathrm{d}\theta} = \mathcal{H}(\mathbf{X}, \mathbf{\Psi}, \sigma, \alpha), \tag{23}$$

where

$$\alpha = (\alpha_1, \alpha_2, ..., \alpha_5)^T,$$

and $\mathbf{\Psi}$ and $\mathbf{X}$ contain the discretized MHD components and the grid points, respectively. After coupling this system to the semi-discretized PDE system (10), a large, stiff, banded, nonlinear ODE system is obtained. System (23) has bandwidth 12. This can be easily derived by working out (20) in terms of the x_i's and realizing that the unknown vector of the complete ODE system is written as $(..., \Psi_i^{(1)}, \Psi_i^{(2)}, ..., \Psi_i^{(5)}, x_i, \Psi_{i+1}^{(1)}, ...)^T$. For the time-integration of this system, the ODE-package DASSL [10] with the (implicit) BDF-methods up to order 5 will be used. DASSL uses a direct solver for the linear systems and exploits the banded form of the equations in the Jacobian formation and numerical linear algebra computations. Numerical differencing for Jacobians in the Newton-process is being used. The time-stepping error tolerance is denoted by *tol* and will be specified at the experiments.

3.3 Numerical results

In what follows, we apply the adaptive method of lines approach to three 1.5D MHD model problems which are chosen to cover significantly diverse challenges typically encountered in numerical MHD simulations. We solve a standard Riemann problem to address the performance of the MOL technique as a shock-capturing and shock-tracing method, we simulate linear

shear Alfvén waves which are non-compressive perturbations with a specific polarization, and we model a plasma-'vacuum' configuration which poses numerical difficulties to keep density and pressure positive throughout the domain. We explicitly compare the obtained adaptive grid solutions with high resolution reference solutions on static, uniform grids. These reference solutions are all calculated with the Versatile Advection Code [14] (VAC, see `http://www.phys.uu.nl/~toth`), and if not stated otherwise, use 1000 grid points and the (approximate) Riemann-solver based Total Variation Diminishing (TVD) scheme with 'minmod' limiting. This shock-capturing, one-step TVD scheme is actually one out of six high resolution spatial discretization schemes available in VAC, and has demonstrated to be the most accurate and efficient discretization method on a large variety of HD and MHD problems [13]. Specifically, the effects of dispersion and diffusion will essentially be minimal in the reference solutions, and this should be kept in mind when comparing them with the adaptive simulation results. For the latter, all experiments used values for the smoothing parameters $\tau = 10^{-5}$, $\sigma = 2$, and $tol = 10^{-6}$. The adaptivity constants will be specified and motivated per model.

3.3.1 MHD-shocktube model

This test problem by [2] and also used in [13] has evolved into a benchmark for MHD codes. The initial Riemann problem separates a high density and high thermal pressure left state from a low density and low pressure right state with the magnetic field lines reflected over the normal to the discontinuity line $x = 0.5$ in the $x - y$ plane. The sudden expansion of the left state produces a reversedly propagating fast rarefaction fan and a slow compound wave, a rightwardly advected contact discontinuity, and a right-moving slow shock and fast rarefaction fan. The compound wave is a combination of a slow shock with a slow rarefaction attached to it.

Specifically, the problem is set up in the space-interval $x \in [0, 1]$, while we simulate for times $t \in [0, 0.1]$. In the adaptive approach, we use 250 grid points, and added artificial diffusion terms $\epsilon \frac{1}{\mathcal{J}} \frac{\partial}{\partial \xi} [\frac{1}{\mathcal{J}} \frac{\partial \mathbf{\Psi}^{(j)}}{\partial \xi}]$ to all but the mass-conservation law with diffusion coefficients $\epsilon = 0.0001$. Since all developing dynamic features have an associated density variation, we set the adaptivity parameter $\alpha_1 = 1$, while all other parameters $\alpha_i = 0, \quad (i = 2, ..., 5)$. Furthermore,

$$\gamma = 2, \qquad \bar{B}_1 \equiv 0.75$$

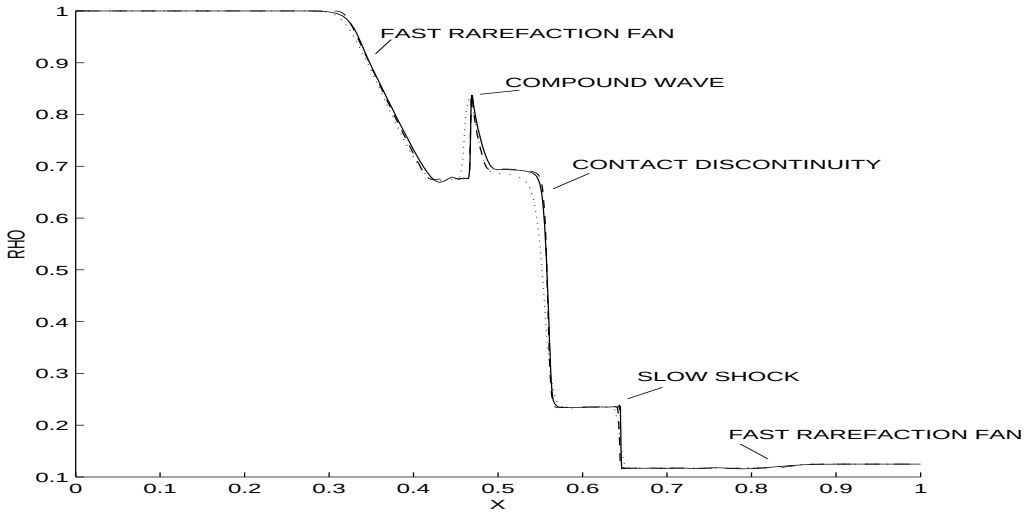

Figure 1: Density at $t = 0.1$ for the magnetic shocktube model. We compare two static grid reference solutions, one with 250 grid points (dots) and one for 1000 grid points (dashed), with an adaptive MOL solution exploiting 250 points (solid).

$$\rho|_{t=0} = \begin{cases} 1 & \text{for } x \in [0, 0.5] \\ 0.125 & \text{for } x \in [0.5, 1] \end{cases}$$

$$m_1|_{t=0} = m_2|_{t=0} = 0$$

$$B_2|_{t=0} = \begin{cases} 1 & \text{for } x \in [0, 0.5] \\ -1 & \text{for } x \in [0.5, 1] \end{cases}$$

$$e|_{t=0} = \begin{cases} 1.78125 & \text{for } x \in [0, 0.5] \\ 0.88125 & \text{for } x \in [0.5, 1] \end{cases}$$

Homogeneous Neumann boundary conditions are used for all components.

In Fig. 1, we compare the density profile at $t = 0.1$ from three simulations: a VAC solution on a 250 point static grid, the adaptive solution with the same amount of grid points, and the true reference VAC solution exploiting 1000 points (both VAC solutions used a Courant number of 0.8). Clearly, the MOL technique is superior to the VAC solution that uses the same amount of grid points, and the accuracy of the adaptive method is identical to the high resolution reference solution. We thus save a factor of 4 in grid resolution as compared to a uniform grid. In Fig. 2, we plot at left the $v_1 := m_1/\rho$

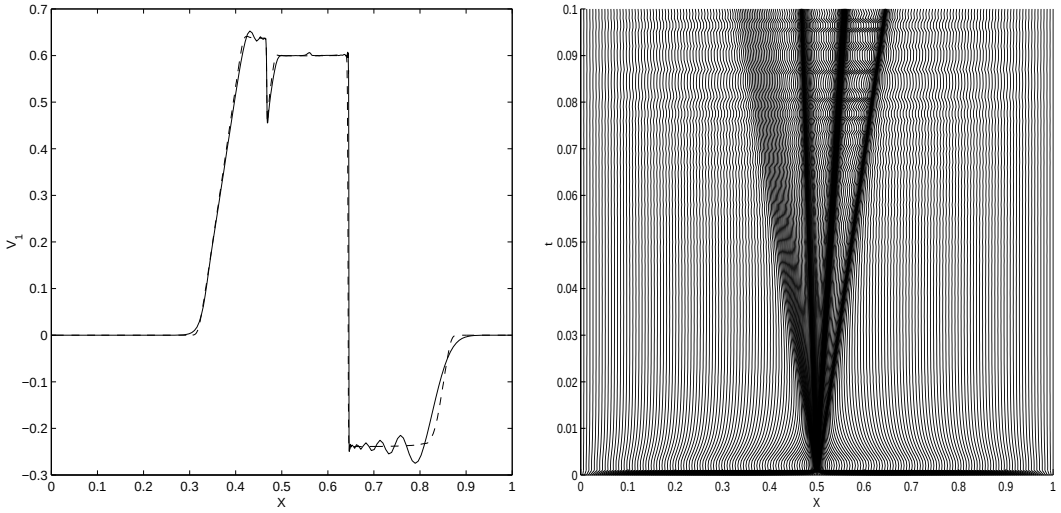

Figure 2: Left panel: v_1 component of the velocity $t = 0.1$ for both the reference (dashed) and the MOL solution (solid). Right panel: grid history (tracing x-positions of grid points as a function of time t) for the magnetic shocktube model.

velocity profile at the same time for both the adaptive and the reference solution, while the grid history for $t \in [0, 0.1]$ is shown at right. Note that the adaptive solution is fairly dispersive for this particular variable. The grid history demonstrates how the initial discontinuity causes an immediate clustering of grid points in the region of interest and that the emerging shock features are nicely traced individually.

3.3.2 Shear-Alfvén waves

This test problem was described by [12] and also used in [13] for their evaluation of different discretization schemes. A homogeneous, uniformly magnetized plasma state is perturbed with a localized velocity pulse transverse ($v_2 := m_2/\rho \neq 0$) to the horizontal (x-direction) magnetic field. This evolves into two oppositely traveling Alfvén waves that only have associated $v_2 := m_2/\rho$ and B_2 perturbations. The complete problem setup is as follows.

We take $x \in [0, 3]$ and time-interval $t \in [0, 0.8]$, together with artificial diffusion coefficients (except for the mass-conservation law) $\epsilon = 0.0001$. Because we only expect transverse vector components, we set the adaptivity

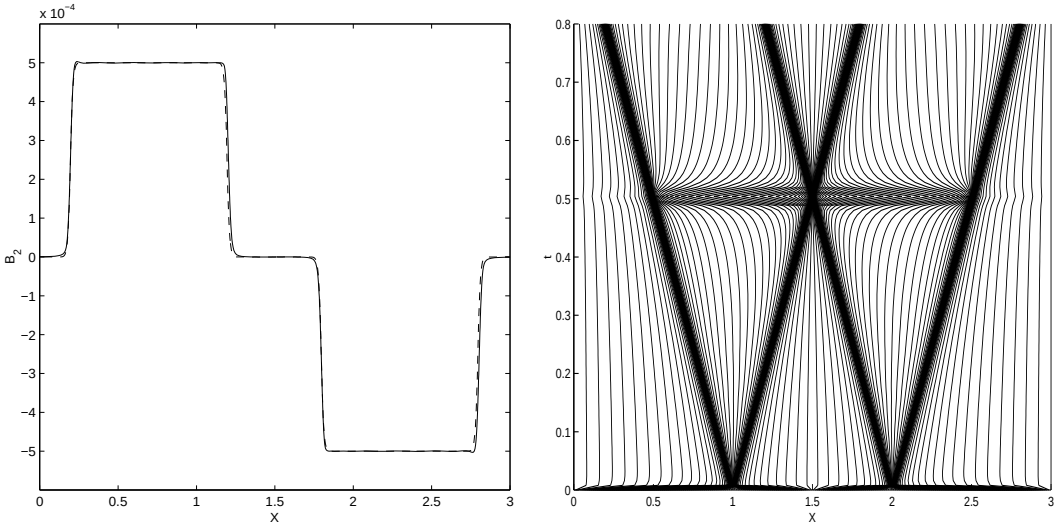

Figure 3: Left panel: y-component of magnetic induction for the Shear-Alfvén problem at $t = 0.8$, again from a 1000 point reference solution (dashed) with a 250 MOL solution. Right panel: grid history for the adaptive simulation.

parameters $\alpha_3 = \alpha_4 = 1e+8$ with all other $\alpha_1 = \alpha_2 = \alpha_5 = 0$. The high values for α_3 and α_4 are a consequence of a scaling effect in the weight function. Since $(\frac{\Delta B_2}{\Delta x})^2 = \mathcal{O}(10^{-8})$ occurs in $\mathcal{W}$, it is natural to choose the adaptivity parameter(s) $\mathcal{O}(10^8)$ to balance the different terms. The number of grid points for this model is taken equal to 250. Physical parameters and initial conditions for this model are:

$$\gamma = 1.4, \qquad \bar{B}_1 \equiv 1$$

$$\rho|_{t=0} = 1$$

$$m_1|_{t=0} = 0$$

$$m_2|_{t=0} = \begin{cases} 10^{-3} & \text{for } x \in [1,2] \\ 0 & \text{elsewhere} \end{cases}$$

$$B_2|_{t=0} = 0$$

$$e|_{t=0} = \begin{cases} 0.5000005025 & \text{for } x \in [1,2] \\ 0.5000000025 & \text{elsewhere} \end{cases}$$

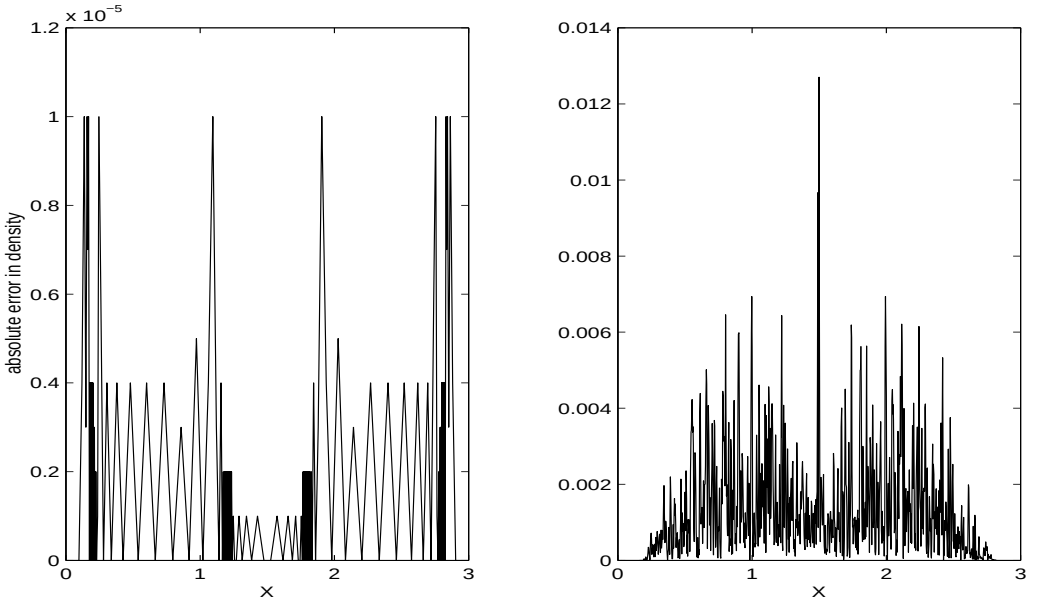

Figure 4: Comparison of the errors in the density profile for the reference MOL approach (left) and the TVD result (right). Note the different scales on the ρ-axes.

Homogeneous Neumann boundary conditions hold for all components.

Figure 3 shows the B_2 component of the magnetic induction at $t = 0.8$ from both the MOL and the reference solution. In the right panel, the grid history is shown. The solution again compares favorably to the high resolution static grid simulation, only slightly worsened by dispersion. The grid history shows how the original single pulse separates into two oppositely traveling signals. In Fig. 4, we compare the errors present for both the reference solution and the adaptive one: ideally the density should remain constant. Noting the large difference in scales, the MOL approach succeeds better in minimizing the density variations. In fact, we used a Courant number of 0.4 for the reference solution in order to suppress these errors somewhat. For the reference result, they are due to the small thermal pressure ($p = 10^{-9}$) which creates roundoff problems within the Riemann solver used (see also [13]). Indeed, when switching to the non-Riemann solver based TVD Lax-Friedrichs discretization in VAC, these errors essentially disappear. Although the MOL solution seems better judged from the controlled density variations, it fails to maintain the positivity of the thermal pressure for this example.

3.3.3 Oscillating plasma sheet

This test model was introduced recently in [15] as a typical case where an implicit time integration strategy is more efficient than explicit methods. A sheet of high density and pressure is surrounded by a magnetized 'vacuum'. The vacuum is modeled as a low density, low pressure plasma so that the plasma-vacuum interface is prone to introduce non-physical negative density and/or pressure fluctuations. We set up an initial total pressure imbalance across the sheet by prescribing a uniform, sheet-aligned magnetic field of different magnitude in the left and right vacuum region. With ideally conducting wall boundary conditions at some distance away from the sheet boundaries, this results in a magnetically controlled oscillation of the sheet as a whole due to alternate compressions and rarefactions of the vacuum magnetic fields on either side.

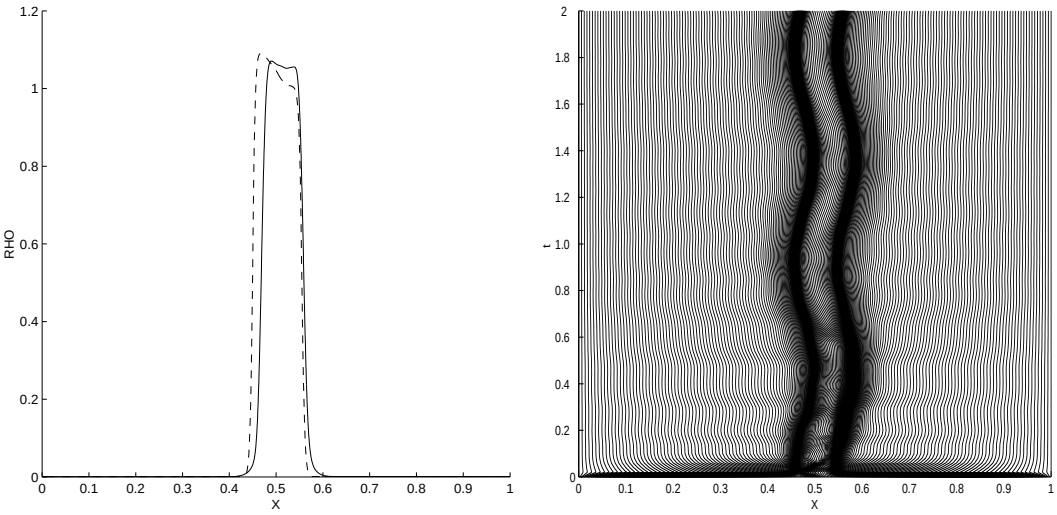

Figure 5: Density at $t = 2$ and grid history until that time for the oscillating plasma sheet. In the left panel, the MOL solution (solid) is again compared with a 1000 grid point reference solution.

Specifically, for $x \in [0,1]$, time $t \in [0,2]$, we now use artificial diffusion coefficients $\epsilon = 0.001$ for momentum, energy and magnetic field, while it was even necessary for stability reasons to introduce an artifical diffusion term in the mass-conservation law with $\epsilon = 10^{-5}$. We took as adaptivity parameters $\alpha_i = 1$ $(i = 1, ..., 5)$ since there is no particular component which

should be emphasized (we could perhaps take $\alpha_3 = 0$ since there will be no v_2 motion induced aligned with the sheet). The MOL solution employed 350 grid points. In summary

$$\gamma = 1.4, \qquad \bar{B}_1 \equiv 0$$

$$\rho|_{t=0} = \begin{cases} 10^{-3} & \text{for } x \in [0, 0.45] \\ 1 & \text{for } x \in [0.45, 0.55] \\ 10^{-3} & \text{for } x \in [0.55, 1] \end{cases}$$

$$m_1|_{t=0} = m_2|_{t=0} = 0$$

$$B_2|_{t=0} = \begin{cases} 1.1 & \text{for } x \in [0, 0.45] \\ 0.6 & \text{for } x \in [0.45, 0.55] \\ 1.0 & \text{for } x \in [0.55, 1] \end{cases}$$

$$e|_{t=0} = \begin{cases} 0.60525 & \text{for } x \in [0, 0.45] \\ 0.98025 & \text{for } x \in [0.45, 0.55] \\ 0.50025 & \text{for } x \in [0.55, 1] \end{cases}$$

Homogeneous Neumann BCs for all components, except for momentum in the x-direction for which $m_1|_{\partial\Omega} = 0$.

In Fig. 5 the density at time $t = 2$, and the grid history until that time is shown. The density panel compares again the adaptive solution with a reference result (with Courant number 0.8), and it can be seen that the solution is somewhat influenced by the higher (artificial) diffusion imposed. From the grid history, we conclude that the timeframe shown is a little over two 'periods' of the induced oscillation, which is in agreement with the estimated period 0.97 as listed in [15]. Note how the MOL technique nicely succeeds in tracing the waving motion of the sheet boundaries. In contrast with the previous example, the adaptive method is able to maintain the positivity of the thermal pressure for this case.

4 Towards 2D MHD modeling

4.1 2D magnetic field evolution

In contrast to the 1D MHD case from above, multi-dimensional MHD simulations face a non-trivial task when advancing a magnetic field configuration

forward in time while ensuring the property $\nabla \cdot \mathbf{B} = 0$. The core problem is represented by the induction equation (4), alternatively written as

$$\frac{\partial \mathbf{B}}{\partial t} = \nabla \times (\mathbf{v} \times \mathbf{B}) + \epsilon_m \Delta \mathbf{B} \tag{24}$$

with ϵ_m the resistivity $\epsilon_m \geq 0$. In two space dimensions, setting $\mathbf{B} = (B_1, B_2, 0)$, we obtain the following system of PDEs,

$$\frac{\partial B_1}{\partial t} = \epsilon_m \Delta B_1 + v_1 \frac{\partial B_2}{\partial y} - v_2 \frac{\partial B_1}{\partial y} + B_2 \frac{\partial v_1}{\partial y} - B_1 \frac{\partial v_2}{\partial y}, \tag{25}$$

$$\frac{\partial B_2}{\partial t} = \epsilon_m \Delta B_2 - v_1 \frac{\partial B_2}{\partial x} + v_2 \frac{\partial B_1}{\partial x} - B_2 \frac{\partial v_1}{\partial x} + B_1 \frac{\partial v_2}{\partial x}, \tag{26}$$

together with the property $\nabla \cdot \mathbf{B} = 0$. This system will be solved using a 2D adaptive grid method in section 4.2.6, with particular attention paid to the solenoidal condition.

One way to ensure a divergence-free magnetic field at all times is to make use of a vector potential formulation where $\mathbf{B} := \nabla \times \mathbf{A}$. In two dimensional applications, the system (25)-(26) is then equivalent to the single PDE for the scalar A_3 component

$$\frac{\partial A_3}{\partial t} = -\mathbf{v} \cdot \nabla A_3 + \epsilon_m \Delta A_3, \tag{27}$$

with $\frac{\partial A_3}{\partial y} = B_1$, $-\frac{\partial A_3}{\partial x} = B_2$, while $\mathbf{A} = (0, 0, A_3)$. We will use this simpler model in section 4.2.4 to compare different means for generating a 2D adaptive grid. Note that magnetic field lines are isolines of this A_3 potential.

Finally, we point out (cfr. [17]) that the partial problem posed by the system (25)-(26), or equivalently the PDE (27), can be relevant as a physical solution to the special case where we consider incompressible flow $\nabla \cdot \mathbf{v} = 0$, the momentum equation (2) under the condition that the magnetic energy $\mathbf{B}^2/2$ is much smaller than the kinetic energy $\rho \mathbf{v}^2/2$, and the induction equation itself. In those circumstances, the momentum balance decouples from the magnetic field evolution. In the model problems studied, we therefore impose an incompressible flow field $\mathbf{v}(x, y)$.

4.2 Adaptive grids in two space dimensions

4.2.1 Transformation in 2D

As in the 1D-case we first make use of a transformation of variables

$$\xi = \xi(x, y, t), \quad \eta = \eta(x, y, t), \quad \theta = t, \tag{28}$$

that yields for the equation (27) (a similar derivation can be made for the (B_1, B_2) system)

$$\begin{aligned}\mathcal{J} A_{3,\theta} + A_{3,\xi}(x_\eta y_\theta - x_\theta y_\eta) + A_{3,\eta}(x_\theta y_\xi - x_\xi y_\theta) \\ = A_{3,\xi}(-v_1 y_\eta + v_2 x_\eta) + A_{3,\eta}(v_1 y_\xi - v_2 x_\xi)\end{aligned}$$

$$\begin{aligned}+\epsilon_m \Bigg[(\frac{x_\eta^2 + y_\eta^2}{\mathcal{J}} A_{3,\xi})_\xi - (\frac{x_\xi x_\eta + y_\xi y_\eta}{\mathcal{J}} A_{3,\eta})_\xi \\ -(\frac{x_\xi x_\eta + y_\xi y_\eta}{\mathcal{J}} A_{3,\xi})_\eta + (\frac{x_\xi^2 + y_\xi^2}{\mathcal{J}} A_{3,\eta})_\eta \Bigg]. \end{aligned} \tag{29}$$

Here, $\mathcal{J} = x_\xi y_\eta - x_\eta y_\xi$ is the determinant of the Jacobian of the transformation. In general, we then allow for truly two-dimensionally deforming grids.

If we restrict the grid adaptation in a 1.5D manner, i.e. when we impose the extra restriction $x_\eta = y_\xi = 0$, we get $\mathcal{J} = x_\xi y_\eta$, and equation (29) simplifies to

$$\begin{aligned} x_\xi y_\eta A_{3,\theta} - A_{3,\xi} y_\eta x_\theta - A_{3,\eta} x_\xi y_\theta &= -v_1 y_\eta A_{3,\xi} - v_2 x_\xi A_{3,\eta} \\ &+ \epsilon_m \Bigg[(\frac{y_\eta A_{3,\xi}}{x_\xi})_\xi + (\frac{x_\xi A_{3,\eta}}{y_\eta})_\eta \Bigg]. \end{aligned} \tag{30}$$

This dimensionally split approach for the grid adaptation will be compared with fully 2D deformations for the model problem from section 4.2.4.

4.2.2 Adaptive grid PDEs in 2D

Due to the 2D-transformation, now two fourth-order PDEs are needed to define the grid and thereby the transformation. As an immediate extension of the 1D-case (11) we set

$$\begin{aligned} [(\mathcal{S}_1(x_\xi) + \tau x_{\xi\theta})\mathcal{W}_1]_\xi = 0, \\ [(\mathcal{S}_2(y_\eta) + \tau y_{\eta\theta})\mathcal{W}_2]_\eta = 0, \end{aligned} \tag{31}$$

with $\mathcal{S}_1$ and $\mathcal{S}_2$ direction-specific versions of the operator $\mathcal{S}$ defined in (12). The weight functions in (31) are now

$$\mathcal{W}_1 = \sqrt{1 + \alpha\ A_{3,x}^2}, \quad \mathcal{W}_2 = \sqrt{1 + \alpha\ A_{3,y}^2}, \tag{32}$$

for a fully 2D adaptive grid, while in the 1.5D case, we set

$$\mathcal{W}_1 = \sqrt{1 + \alpha \max_y A_{3,x}^2}, \quad \mathcal{W}_2 = \sqrt{1 + \alpha \max_x A_{3,y}^2}. \tag{33}$$

It can be shown (using 1D arguments in two directions), that with the latter choice

$$\mathcal{J} = x_\xi y_\eta > 0, \qquad \forall\, \theta \geq 0, \tag{34}$$

so that this restricted grid adaptivity maintains the desirable property that grid cells do not fold over. For the more general case (32), no guarantee can be given that grid points will not collide! This could be called the 'battle between adaptivity and regularity'. The method parameters τ, σ, α are chosen in a similar way as before and are specified per problem in the following sections. After semi-discretization of (30) and (31) we end up with a banded ODE-system with bandwidth $= 6 * npts + 2$, where $npts \times npts$ denotes the total number of gridpoints in 2D. This ODE-system is again time-integrated with DASSL [10].

4.2.3 Numerical results

4.2.4 Kinematic flux expulsion

This model problem dates back to 1966 [17], as one of the first studies to address the role of the magnetic field in a convecting plasma. Starting from a uniform magnetic field, its distortion by cellular convection patterns was simulated numerically for various values of the resistivity ϵ_m. We use this model problem to compare the 2D with the 1.5D approach for two-dimensional moving grids.

Our 2D kinematic flux expulsion uses an imposed four-cell convection pattern with its incompressible velocity field given by

$$\mathbf{v}(x, y) = (\sin(2\pi x)\cos(2\pi y), -\cos(2\pi x)\sin(2\pi y)).$$

We solve for the scalar vector potential A_3 from (27) on the domain $(x, y) \in [0, 1] \times [0, 1]$ and for times $t \in [0, 0.5]$. We set the adaptivity parameter α to unity, and $\tau = 10^{-3}, \sigma = 1$. The grid dimension is 25×25, while the resistivity is set equal to $\epsilon_m = 0.005$. In terms of A_3, the initial uniform vertical field is obtained through $A_3|_{t=0} = 1 - x$, while the boundary conditions are

$$A_3|_{x=0} = 1, \; A_3|_{x=1} = 0, \; A_3|_{y=0} = A_3|_{y=1}.$$

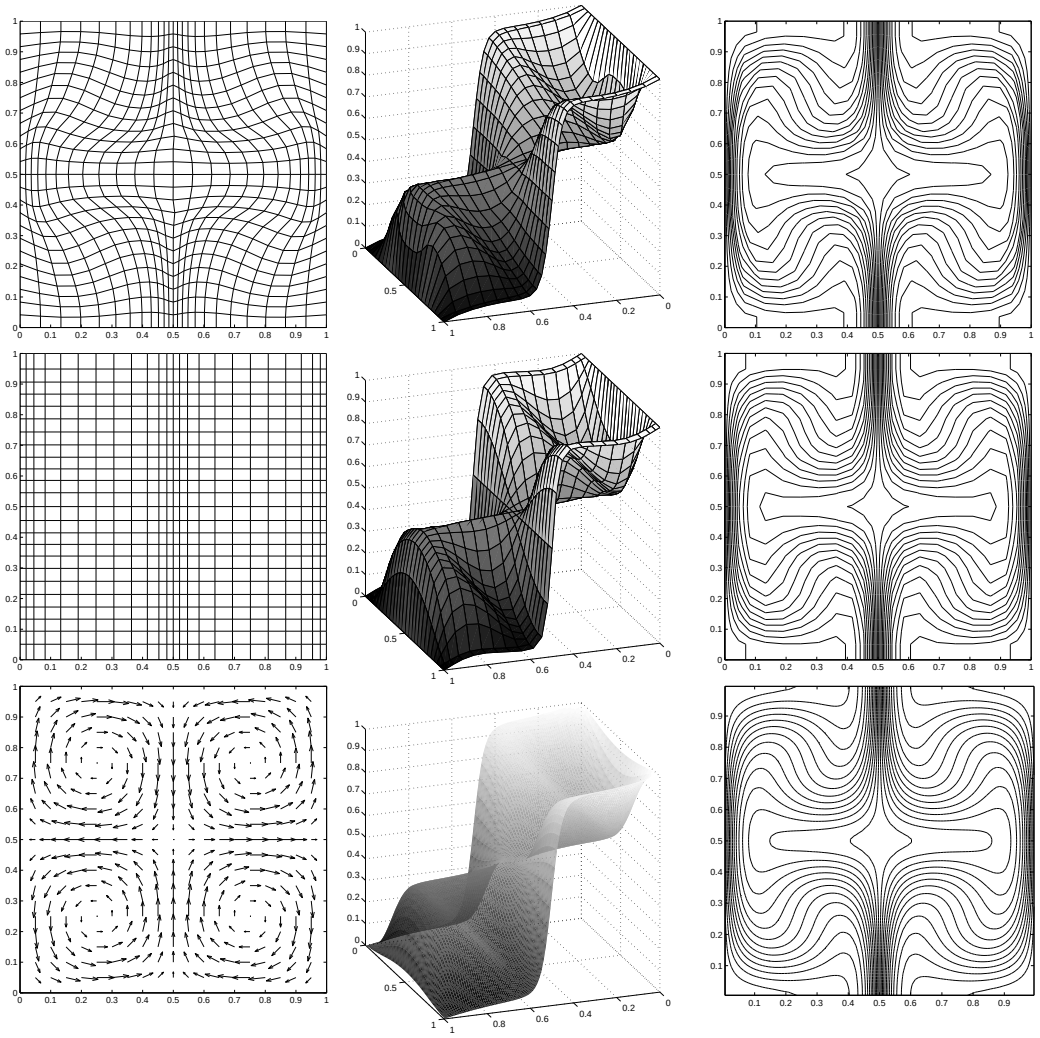

Figure 6: Three solution strategies for 2D kinematic flux expulsion compared: each row shows for time $t = 0.5$ the grid, the solution for the vector potential $A_3(x, y)$ as a surface plot, and as a contourplot (showing magnetic field lines) with fixed contour levels at $A_3 = 0 : 0.05 : 1$. Top row uses a 25×25 two-dimensionally deforming grid, middle row uses restricted 1.5D adaptivity, bottom row is a 100×100 reference solution. The imposed velocity field is depicted at bottom left.

In Fig. 6, we compare the grids and the obtained solution $A_3(x, y)$ at time $t = 0.5$ for three simulation results. The top row uses a full 2D grid deformation, the middle row takes the 1.5D adaptivity approach, while the bottom row shows a reference VAC solution on a 100×100 uniform, static grid. The solution is both shown as a surface and a contour plot, with the contour values varying between 0 and 1 with steps of 0.05. Note that the 1.5D deformation works well for this case, since the steep parts of the solution mostly vary in the x-direction. Although the 2D-grid shows slightly sharper contour lines in the middle of the domain, the 2D deformation may breakdown at some point of time. For both cases we gain a factor of 16 in the total number of grid points compared with the reference solution.

4.2.5 Advection of a current-carrying-cylinder

To demonstrate the dimensionally split grid adaption on a case where truly 2D deformations are required, we solve for the circular advection of a current-carrying cylinder (taken from [13]).

With a computational domain of size $(x, y) \in [-50, 50] \times [-50, 50]$, we embed an isolated magnetic 'flux tube' in a circulatory flow. The cylinder is specified by

$$A_3|_{t=0} = \begin{cases} R/2 - [(x - x_0)^2 + (y - y_0)^2]/2R & \text{if } (x - x_0)^2 + (y - y_0)^2 < R^2, \\ 0 & \text{elsewhere,} \end{cases}$$

and is initially centered at $(x_0, y_0) = (0, 25)$ with radius $R = 15$ and the magnetic field strength increases radially from zero to one at the cylinder edge. In terms of a current $\mathbf{J} = \nabla \times \mathbf{B}$, the cylinder has a constant axial current throughout.

We simply rotate this current-carrying cylinder around (counterclockwise) by imposing

$$\mathbf{v}(x, y) = (-y, x).$$

When we solve for times $t \in [0, 2\pi]$, we then follow one period of revolution of the cylinder, at which time the initial configuration must be regained. The method parameters are: adaptivity parameter $\alpha = 200$ (due to the scaling-effect), $\tau = 10^{-3}$, $\sigma = 1$. We now use the dimensionally decoupled adaptivity on a 25×25 grid and a dimensionless artificial diffusion of 0.5×10^{-4}. Boundary conditions do not play a role in this example, so we simply took homogeneous Dirichlet conditions $A_3|_{\partial\Omega} = 0$ everywhere. In Fig. 7 we see

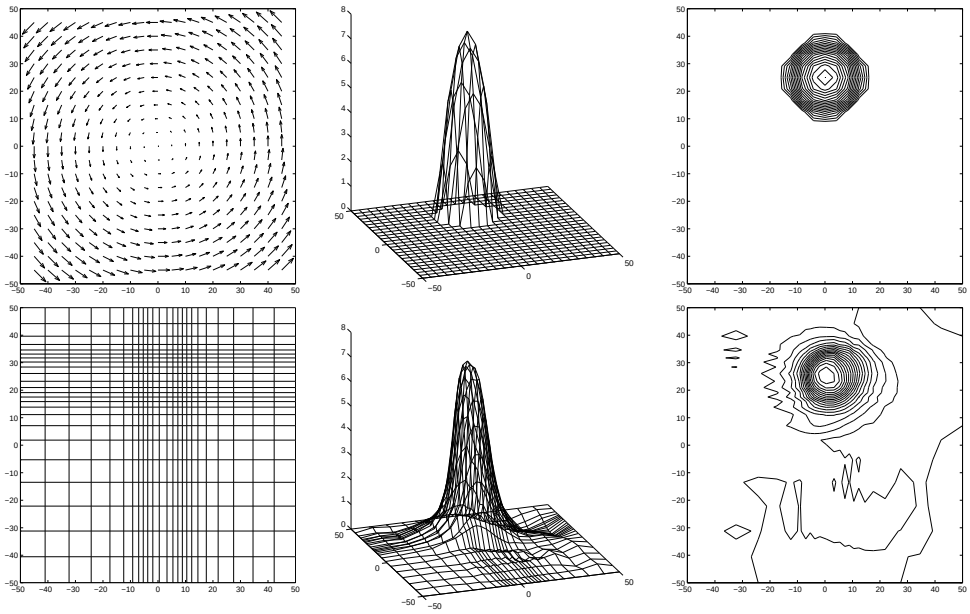

Figure 7: For initial time $t = 0$ (top row) and after one rotation at time $t = 2\pi$ (bottom row): Grid, surface plot of the potential A_3, and magnetic field lines for the current-carrying cylinder model with fixed contour levels at $A_3 = 0 : 0.325 : 7.5$. The top left frame shows the imposed circulation as a vector field.

the grids, solutions, and contourplots at $t = 2\pi$. The adaptive grid is nicely situated around the cylinder, although the solution is slightly smoothed by the artificial diffusion term, which can also be seen in the contourplot.

4.2.6 Conservation of $\nabla \cdot \mathbf{B} = 0$?

To investigate how the adaptive method copes with the important property $\nabla \cdot \mathbf{B} = 0$, we now take the full (B_1, B_2) system given by (25)-(26). Note that the current-carrying-cylinder model is not appropriate for this purpose, since the initial condition for the (B_1, B_2) system consists of piecewise linear parts (this follows from the initial condition for A_3 and $\mathbf{B} := \nabla \times \mathbf{A}$). As a consequence, *constant* weight functions W_1 and W_2 are obtained and therefore a uniform grid for all $t \geq 0$, independent of the choice of the adaptivity parameter α. For this reason, we examine the (B_1, B_2) version of the model in 4.2.4 with initial conditions $B_1|_{t=0} = 0$, $B_2|_{t=0} = 1$ and periodic boundary

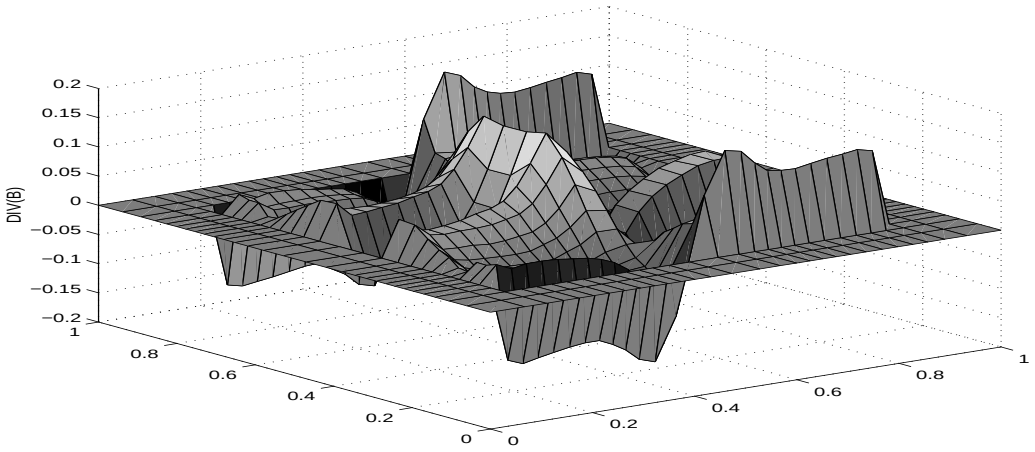

Figure 8: The divergence of the magnetic field for the solution in (4.2.6) at time $t = 0.1$ on a 30×30 adaptive grid. We evaluated the divergence from a centered difference formula.

conditions. For simplicity we take the 1.5D approach. In Fig. 8, we show a plot of $\nabla \cdot \mathbf{B} = 0$ on a 30×30 adaptive grid at $t = 0.1$, as evaluated from a central difference discretization:

$$[\nabla \cdot \mathbf{B} = 0]_{i,j} \approx \frac{B_{1,i+1,j} - B_{1,i-1,j}}{x_{i+1} - x_{i-1}} + \frac{B_{2,i,j+1} - B_{2,i,j-1}}{y_{j+1} - y_{j-1}}.$$

Numerical values of $||\nabla \cdot \mathbf{B}||_\infty$ for different grid sizes are: 0.2117 (on a 20×20 grid), 0.2104 (25×25 grid), and 0.1743 (30×30 grid). The main conclusion from these results is that, although the grid concentrates near areas of high-spatial activity, the solenoidal condition on the magnetic field is not preserved satisfactorily at all. This is a severe drawback of the current method-of-lines implementation. A possible remedy for this could be adding a projection scheme after every time step, i.e. applying a Poisson solver to correct the divergence of the magnetic field [1].

5 Conclusions

In this paper we applied the adaptive method-of-lines technique to various 1D MHD problems and 2D magnetic field evolution simulations. In 1D, accurate numerical results were obtained for three important test cases. The

method could further benefit from specific MHD properties that have not been exploited in the present implementation. For the 2D case, the adaptive method with restricted grid motion performed comparable to fully 2D adaptive simulations. This is of interest for easier generalizations to 3D calculations. Future work will consist of fully 2D MHD simulations and 3D applications (model problems could e.g. be taken from [6], [9]). From our results, it is clear that attention should be paid to means of maintaining pressure positivity in very low pressure situations, more physically based artificial diffusion terms, and an appropriate remedy for ensuring the solenoidal condition on the magnetic field vector in combination with the adaptive grid method for multi-dimensional applications. To allow for the latter applications, we will switch to the use of iterative methods for the linear systems behind the Newton-process in the stiff ODE-solver.

References

[1] J. U. Brackbill & D. C. Barnes, The effect of nonzero $\nabla \cdot \mathbf{B}$ on the numerical solution of the magnetohydrodynamic equations, *J. Comput. Phys.* **35** (1980), 426-430.

[2] M. Brio & C. C. Wu, An upwind difference scheme for the equations of ideal magnetohydrodynamics, *J. Comput. Phys.* **75** (1988), 400-422.

[3] E. A. Dorfi & L. O.'Drury, Simple adaptive grids for 1-D initial value problems, *J. Comput. Phys.* **69**(1987), 175-195.

[4] H. Friedel, R. Grauer & C. Marliani, Adaptive mesh refinement for singular current sheets in incompressible magnetohydrodynamic Flows, *J. Comput. Phys.* **134**(1997), 190-198.

[5] W. Huang & R. D. Russell, Analysis of moving mesh partial differential equations with spatial smoothing, *Research report* **93-17**(1993), Mathematics and Statistics, Simon Fraser University, Burnaby, British Columbia.

[6] R. Keppens, G. Tóth, R.H.J. Westermann, J.P. Goedbloed, Growth and saturation of the Kelvin-Helmholtz instability with parallel and antiparallel magnetic fields, *J. Plasma Phys.* **61**(1999), 1-19.

[7] R. Keppens, M. Nool, P.A. Zegeling & J.P. Goedbloed, Dynamic grid adaptation for computational magnetohydrodynamics, *Lecture Notes in Computer Science* **1823**(2000), Springer Verlag, 61-70.

[8] R. L. LeVeque, D. Mihalas, E. A. Dorfi & E. Müller, Computational methods for astrophysical fluid flow, *Saas-Fee Advanced Course* **27**(1998), lecture notes 1997, Swiss Society for Astroph. and Astron., Eds. O. Steiner & A. Gautschy, Springer Verlag.

[9] M. G. Linton, G. H. Fisher, R. B. Dahlburg & Y. Fan, Relationship of the multimode kink instability to δ-spot formation, *Astrophys. J.* **522**(1999), 1190-1205.

[10] L. R. Petzold, A description of DASSL: A differential/algebraic system solver, *IMACS Transactions on Scientific Computation*(1983), R. S. Stepleman et al (ed.), North-Holland, Amsterdam, 65-68.

[11] W. E. Schiesser, The numerical method of lines, integration of partial differential equations, *Academic Press, Inc.*(1991), San Diego.

[12] J. M. Stone & M. L. Norman, ZEUS-2D: a radiation magnetohydrodynamics code for astrophysical flows in two space dimensions. II. The magnetohydrodynamic algorithms and tests, *Astrophys. J. Suppl.* **80**(1992), 791-818.

[13] G. Tóth & D. Odstrčil, Comparison of some flux corrected transport and total variation diminishing numerical schemes for hydrodynamic and magnetohydrodynamic problems, *J. Comput. Phys.* **128**(1996), 82-100.

[14] G. Tóth, A general code for modeling MHD flows on parallel computers: Versatile Advection Code,*Astrophys. Lett. & Comm.* **34**(1996), 245-250.

[15] G. Tóth , R. Keppens & M.A. Botchev, Implicit and semi-implicit schemes in the Versatile Advection Code: numerical tests, *Astron. & Astroph.* **332**, 1159-1170.

[16] R. A. Trompert, Local uniform grid refinement for time-dependent partial differential equations, *CWI-tract* **107**(1995), Centrum voor Wiskunde en Informatica, Amsterdam.

[17] N. O. Weiss, The expulsion of magnetic flux by eddies, *Proc. of Roy. Soc. A* **293**(1996), 310-328.

[18] P. A. Zegeling, Moving grid methods for time-dependent partial differential equations, *CWI-tract* **94**(1993), Centrum voor Wiskunde en Informatica, Amsterdam.

[19] P. A. Zegeling, r-refinement for evolutionary PDEs with finite elements or finite differences, *Appl. Num. Maths.* **26**(1998), 97-104.

[20] U. Ziegler, A three-dimensional Cartesian adaptive mesh code for compressible magnetohydrodynamics, *Comp. Phys. Comm.* **116**(1999), 65-77.

Acknowledgements

RK performed his work as part of the research program of the association agreement of Euratom and the 'Stichting voor Fundamenteel Onderzoek der Materie' (FOM) with financial support from the 'Nederlandse Organisatie voor Wetenschappelijk Onderzoek' (NWO) and Euratom. This work was partly performed in the project on 'Parallel Computational Magneto-Fluid Dynamics', funded by the Dutch Science Foundation (NWO) Priority Program on Massively Parallel Computing,